Aeroelastic prediction of the limit cycle oscillations of a cropped delta wing

P.J. Attar*, R.E. Gordnier

Air Force Research Laboratory, AFRL/VAAC, 2210 Eighth St., Bldg 146, WPAFB, OH 45433-7512, USA

Abstract

The flutter and limit cycle oscillation (LCO) behavior of a cropped delta wing are investigated using a newly developed computational aeroelastic solver. This computational model includes a well-validated Euler finite difference solver coupled to a high-fidelity finite element structural solver. The nonlinear structural model includes geometric nonlinearities which are modelled using a co-rotational formulation. The LCOs of the cropped delta wing are computed and the results are compared to previous computations and to experiment. Over the range of dynamic pressures for which experimental results are reported, the LCO magnitudes computed using the current model are comparable to those from a previous computation which used a lower-order von Karman structural model. However, for larger dynamic pressures, the current computational model and the model which used the von Karman theory start to differ significantly, with the current model predicting larger deflections for a given dynamic pressure. This results in a LCO curve which is in better qualitative agreement with experiment. Flow features which were present in the previous computational model such as a leading edge vortex and a shock wave are enhanced in the current model due to the prediction of larger deflections and rotations at the higher dynamic pressures.
© 2005 Elsevier Ltd. All rights reserved.

Keywords: Nonlinear aeroelasticity; Computational aeroelasticity

1. Introduction

The problems caused by moderate to large magnitude static and/or oscillating deflections often are a limiting factor in the design of many aircraft, both military and commercial. A particularly troublesome form of structural response is wing flutter. Wing flutter is a self-excited instability which will cause an infinitesimal wing disturbance to grow exponentially and is caused by the exchange of energy from the surrounding fluid to the structure. If the wing response has a limiting amplitude this is called a limit cycle oscillation (LCO). The limiting of the oscillation amplitude is due to the presence of nonlinearity in the aeroelastic system: fluid, structural or both.

In recent years LCO has been studied both experimentally and theoretically for various Mach number ranges and using models, both aerodynamic and structural, which vary in fidelity. For low subsonic Mach numbers Tang et al. (1999), Tang and Dowell (2001) and Attar et al. (2003a, b) have studied the flutter and LCOs of a moderately swept delta wing using potential flow theory for the aerodynamic modelling and a von Karman plate theory for the nonlinear

---

*Corresponding author. Tel.: +1 937 255 0057; fax: +1 937 656 7857.

E-mail addresses: peter.attar@wpafb.af.mil (P.J. Attar), raymond.gordnier@wpafb.af.mil (R.E. Gordnier).

Nomenclature		u, v, w	flow velocity components in x, y and z
		V_{el}	elemental volume
E	total specific energy	x, y, z	physical coordinates
$\hat{F}, \hat{G}, \hat{H}$	inviscid flux vectors	$\varepsilon_x, \varepsilon_y, \gamma_{xy}$	x, y and shear structural strain components
J	transformation Jacobian	ξ, η, ζ	computational fluid coordinates
t	nondimensional time, $t = tu_\infty/c$	ρ	flow density

structural modelling. They have also performed experiments. Their work showed that LCOs can be caused by structural nonlinearity alone. While their computational model was accurate in the prediction of the zero angle of attack flutter speed, both the nonzero angle of attack flutter speed prediction and the zero and nonzero angle of attack LCO magnitude predictions were not as accurate.

Gordnier studied the zero angle of attack LCO of a moderately swept cropped delta wing in high subsonic flow (Gordnier, 2003). In this work, the computational aeroelastic model consisted of a finite element solution of the nonlinear von Karman plate equations coupled to both an Euler and Navier–Stokes aerodynamic model. For the wing-configuration and Mach number range studied, Gordnier found that viscous effects were limited. However, like the results of Tang and Dowell, the prediction of the LCO amplitudes were not accurate when compared to the experimental results of Schairer and Hand (1997).

In an extension of the work of Tang et al. (1999) and Attar et al. (2003a), Attar et al. (2004a, b) used a higher fidelity structural theory to model the LCO of the delta wing configuration. Here a co-rotational theory is used to compute the structural stiffness of the system. In this work, much better correlation between experiment and theory was noted for both the nonzero angle of attack flutter characteristics and zero and nonzero angle of attack LCO amplitude predictions.

In the work to be performed, the LCO of the delta wing configuration used in Gordnier (2003) will be studied using the Euler fluid model of Gordnier (2003) coupled to the high-fidelity structural model used in Attar et al. (2004b). This combination will provide higher fidelity models for both the aerodynamics and the structural response. The computed LCO results will be compared to the experimental results of Schairer and Hand (1997) and to the previous computations of Gordnier (2003).

2. Theory

2.1. Aerodynamic equations of motion

The aerodynamic governing equations are the unsteady, compressible, three-dimensional Euler equations written in nondimensional, strong-conservation law form (Pulliam and Steger, 1980) employing a general time-dependent transformation. The resulting system of governing equations is expressed as

$$\frac{\partial \hat{U}}{\partial t} + \frac{\partial \hat{F}}{\partial \xi} + \frac{\partial \hat{G}}{\partial \eta} + \frac{\partial \hat{H}}{\partial \zeta} = 0. \tag{1}$$

With this formulation, the vector of dependent variables $\hat{U}$ is given as

$$\hat{U} = \frac{1}{J} U = \frac{1}{J} [\rho \ \ \rho u \ \ \rho v \ \ \rho w \ \ \rho E]^{\mathrm{T}}. \tag{2}$$

All variables have been normalized by the appropriate combination of freestream density, velocity and a characteristic length. The perfect gas relationship closes the system of equations. Previous work with this delta wing (Gordnier, 2003) showed that an Euler calculation is sufficient to capture the primary vortical flow features resulting from flow separation from the sharp leading edge.

2.2. Discretization of the aerodynamic equations of motion

Solutions of Eq. (1) are obtained numerically using the implicit approximately factored finite-difference algorithm of Beam and Warming (1978), employing a Newton-like subiteration procedure (Gordnier and Visbal, 1991). Second-order temporal accuracy is secured in this iterative approach by selecting $\phi = 1/2$ in Eq. (3). The numerical algorithm is

written in approximately factored, delta form as

$$
\left[J^{-1^{p+1}} + \phi^i \Delta t_s \delta_\xi \left(\frac{\partial \hat{F}^p}{\partial U} \right) \right] J^{p+1} \left[J^{-1^{p+1}} + \phi^i \Delta t_s \delta_\eta \left(\frac{\partial \hat{G}^p}{\partial U} \right) \right] J^{p+1} \left[J^{-1^{p+1}} + \phi^i \Delta t_s \delta_\zeta \left(\frac{\partial \hat{H}^p}{\partial U} \right) \right] \Delta U
$$

$$
= -\phi^i \Delta t_s \left[J^{-1^{p+1}} \frac{(1+\phi) U^p - (1+2\phi) U^n + \phi U^{n-1}}{\Delta t} - U^p \left(\left(\frac{\xi_t}{J} \right)_\xi + \left(\frac{\eta_t}{J} \right)_\eta + \left(\frac{\zeta_t}{J} \right)_\zeta \right)^{p+1} \right.
$$

$$
\left. + \delta_\xi(\hat{F}^p) + \delta_\eta(\hat{G}^p) + \delta_\zeta(\hat{H}^p) \right],
\tag{3}
$$

where

$$
\phi^i = \frac{1}{1+\phi}, \quad \Delta U = U^{p+1} - U^p.
\tag{4}
$$

For $p = 1$, $U^p = U^n$ and as $p \to \infty$, $U^p \to U^{n+1}$. In the above expression the geometric conservation law (GCL)

$$
\frac{\partial J^{-1}}{\partial t} + \left(\frac{\xi_t}{J} \right)_\xi + \left(\frac{\eta_t}{J} \right)_\eta + \left(\frac{\zeta_t}{J} \right)_\zeta = 0
\tag{5}
$$

has been used to evaluate the term $(\partial J / \partial t)^{-1}$. This insures satisfaction of the GCL for moving meshes.

With this subiteration approach the right-hand side of Eq. (3) represents the numerical approximation to the governing equation, while the left-hand side vanishes as $p \to \infty$. The left-hand side, therefore, may be modified without loss of formal accuracy, provided a sufficient number of subiterates is employed. In particular, diagonalizing the left-hand side of Eq. (3) following the approach of Pulliam and Chaussee (1981) improves the efficiency of the algorithm. Although the diagonalized form of the ADI scheme is only first-order time-accurate, when coupled with subiterations, higher-order time accuracy may be recovered (Morton et al., 1997). Furthermore, a time step on the left-hand side of the equation Δt_s, may be chosen independently from the physical time step Δt on the right-hand side, thereby enhancing stability. The right-hand side of Eq. (3) may also be modified to include a higher-order, upwind-biased algorithm [Roe scheme (Gaitonde et al., 1995)], lagged boundary conditions or lagged turbulence modelling without destroying the implicit nature of the algorithm.

In Eq. (3) all spatial derivatives are approximated by second-order accurate central differences, and common forms of both implicit and explicit nonlinear dissipation (Jameson et al., 1981) are employed in order to preserve numerical stability. The temporal metric derivatives are discretized in a manner consistent with the temporal derivative of the conserved variables in Eq. (3).

When solving fluid/structure interaction problems, the aerodynamic mesh must be allowed to move in accordance with the motion of the structural surface. In this work, a simple algebraic method described in Melville et al. (1997) deforms the aerodynamic mesh to accommodate the changing surface position. This grid motion strategy has proved adequate for the moderate size wing deflections considered in the present work.

2.3. Structural equations of motion

The ANSYS commercial finite element code (ANSYS, 2002) is used as the nonlinear structural solver in this work. This code uses the principle of virtual work in combination with a Rayleigh–Ritz solution in the form of finite element analysis, to develop a system of nonlinear differential equations. The general form of the equations, in matrix notation, are

$$
[M]\{\ddot{u}\} + [C]\{\dot{u}\} + [K]\{u\} = \{F\},
\tag{6}
$$

where $\{u\}$ is the vector of nodal degrees of freedom, $[M]$, $[C]$ and $[K]$ are the mass, damping and stiffness matrices, respectively, and $\{F\}$ is the vector of applied loads, which in this analysis are due to pressure on the wing. Note that since geometric nonlinearities are to be included in this analysis, the stiffness matrix is a function of the nodal displacements. Also, a Rayleigh damping model is used here so the damping is written as a linear combination of the mass and stiffness matrices.

The geometric nonlinearity due to large deflection/large rotation is modelled here using a co-rotational approach. In this method, a local coordinate system is attached to each element which rotates and translates with the element as deformation takes place. The original element coordinate system stays fixed and the element deformation can therefore be decomposed into a component due to rigid body motion and a component which induces strain. This decomposition

is applied using a matrix transformation

$$[B_l] = [B][T_l], \tag{7}$$

where $[B_l]$ is the nonlinear strain–displacement matrix, $[B]$ is the small strain–displacement matrix written in the original element coordinate system, and $[T_l]$ is the orthogonal transformation matrix which relates the original element coordinates to the local coordinates. The convected coordinate frame differs from the original frame by the amount of rigid body rotation. Therefore, the transformation matrix $[T_l]$ is computed by separating the rigid body deformation from the total deformation using a polar decomposition.

In the current work, a consistent elemental tangent stiffness matrix, $[K_{el}]$, is used. To compute the stiffness in a consistent manner refers to the derivation of the stiffness directly from the discretized finite element equilibrium equations without the introduction of any approximations. The method of computing a consistent tangent stiffness used here is one first developed by Omid and Rankin (1991). With this method no limitation is placed on the largeness of the rotation which can be modelled accurately.

Using the consistent approach of Nour-Omid and Rankin (1991), the element tangent stiffness matrix can be written in the following manner:

$$[K_{el}]^T = \frac{\partial \{F_{int}\}}{\partial \{u\}} = [T_l]^T \int_{V_{el}} [B]^T \frac{\partial \{\sigma\}}{\partial \{u\}} \, dV_{el} + [T_l]^T \int_{V_{el}} \frac{\partial [B]^T}{\partial \{u\}} \{\sigma\} \, dV_{el} + \frac{\partial [T_o]}{\partial \{u\}} \int_{V_{el}} [B]^T \{\sigma\} \, dV_{el}, \tag{8}$$

where $\{F_{int}\}$ is the element internal force vector, $[T_o]$ is the transformation matrix from the original element coordinate system (before any deformation takes place) to the global Cartesian coordinate system, and $\{\sigma\}$ is the vector of element stresses. The first integral in Eq. (8) is the main tangent stiffness matrix and the second and third integrals are due to stress stiffening. The full "structure size" stiffness matrix $[K]$ used in Eq. (6) is assembled from the elemental stiffnesses in the usual manner.

The stress-stiffness terms in Eq. (8) are computed using the nonlinear Green strain–displacement relationships:

$$\varepsilon_x = \frac{\partial u_x}{\partial x} + \frac{1}{2}\left[\left(\frac{\partial u_x}{\partial x}\right)^2 + \left(\frac{\partial u_y}{\partial x}\right)^2 + \left(\frac{\partial u_z}{\partial x}\right)^2\right], \tag{9}$$

$$\varepsilon_y = \frac{\partial u_y}{\partial y} + \frac{1}{2}\left[\left(\frac{\partial u_x}{\partial y}\right)^2 + \left(\frac{\partial u_y}{\partial y}\right)^2 + \left(\frac{\partial u_z}{\partial y}\right)^2\right], \tag{10}$$

$$\gamma_{xy} = \frac{\partial u_x}{\partial y} + \frac{\partial u_y}{\partial x} + \left[\frac{\partial u_x}{\partial x}\frac{\partial u_x}{\partial y} + \frac{\partial u_y}{\partial x}\frac{\partial u_y}{\partial y} + \frac{\partial u_z}{\partial x}\frac{\partial u_z}{\partial y}\right]. \tag{11}$$

The above model differs from the von Karman structural model in its assumption about the largeness of rotations. The von Karman model is derived based on the premise that the angles of rotation of the elements of a thin plate are small in comparison to unity. With this assumption it can be shown (Novozhilov, 1953) that all nonlinear terms which contain derivatives of the in-plane displacements (u_x and u_y) in the equations for the strain components (mid-plane components and components which vary through the thickness) can be neglected. In the co-rotational model described in this section, no assumption is made about the largeness of rotations. The only assumption that is made in the above-described model is that of small strain (strain much less than unity).

Shell elements were used to discretize the structural domain. The type of shell element used is a four-noded element with six degrees of freedom per node. The in-plane displacements for this element are modelled using the shape functions for a four-node plane element with extra nodes, often called a QM6 element (Cook et al., 2002). The out-of-plane deflection u_z and two in-plane rotations θ_x and θ_y are modelled using a form of the discrete Kirchhoff plate element. The shell drilling degree of freedom, θ_z, is given a small stiffness to alleviate any numerical problems.

The full system of structural equations, Eq. (6), is solved using a Newton–Raphson iteration to solve the nonlinear equations at each instant in time and the average acceleration form of the implicit Newmark family of integration methods is used to advance the structural solution forward in time. The average acceleration Newmark method has second-order temporal accuracy.

2.4. Fluid–structure coupling

In order to model the aeroelastic phenomena, the structural model and aerodynamic model must be coupled. In the structural equation, Eq. (6), this coupling is due to the pressure load vector $\{F\}$. In the aerodynamic system, the coupling comes from the resulting wing deflection u_z.

In order to achieve implicit coupling of the aerodynamic and structural equations, the subiteration procedure described in Section 2.2 is replaced with a global subiteration. During each subiteration the aerodynamic forces on the structure are updated and the aerodynamic mesh is moved using updated structural displacements. The use of a subiteration procedure to implicitly couple the two physics models reduces any temporal lag which may have existed due to the loose coupling of the models. Complete synchronization of the equation sets is achieved through the subiteration procedure. The importance of synchronizing the loosely coupled systems was demonstrated in Gordnier and Visbal (2002). The fluid solver factorization and linearization errors are also eliminated using the global subiteration strategy. The resulting coupled procedure retains second-order temporal accuracy.

In the current work, the baseline computational model used the same distribution of grid points on the surface of the wing for the aerodynamic grid and the structural grid. LCO results were also computed at the highest dynamic pressure for two other structural grids. These grids were unstructured, with topologies which did not match the aerodynamic grid, and therefore interpolation of the pressures and displacements between the structural and aerodynamic grids was necessary. This interpolation was accomplished using a thin-plate spline algorithm.

3. Results

Shown in Fig. 1 is a schematic of the cropped delta wing configuration which will be modelled in this work. The semispan delta wing configuration is based on the experimental model of Schairer (Schairer and Hand, 1997). The wing is constructed from 0.035 in. thick, cold-rolled steel and has $47.8°$ leading edge sweep and $-8.7°$ trailing edge sweep. The leading edge, trailing edge and wingtip are all blunt. The material properties of the wing used in the computational work are: mass density of 0.283 lbm/in^3,[1] Young's modulus of 30×10^6 lbf/in^2 and a Poisson's ratio of 0.25. The model is assumed to be rigidly clamped along the full root chord of the wing. Fig. 2 shows the first three structural modes for this configuration.

The aerodynamic grid used in the work consists of 141 points in the axial direction (x), 109 points in the spanwise direction (y) and 161 points in the normal direction (z). The delta wing is centered in the mesh in the normal direction with 82 points located above and below the wing. In the aerodynamic model, the thickness of the wing is taken to be the minimum spacing of the grid at the wall, $\Delta z = 0.00005$. The grid extends 2 characteristic lengths upstream, downstream and in the normal direction. In the spanwise direction the grid boundary is located approximately 2.8 span lengths from the tip of the delta wing.

For the baseline aeroelastic model used in the current work, the distribution of the structural nodes is chosen to coincide with the surface distribution of the aerodynamic grid points. This was done in order to eliminate the added complication caused by the interpolation of deflections and forces back and forth between dissimilar computational grids. This resulted in the structural model containing a total of 3600 quadrilateral shell elements. Two different unstructured meshes, which contained fewer and better shaped elements, were also used to compute the LCO results at the largest dynamic pressure of 5.46 psi(lb/in^2). For these cases a thin-plate spline method was used to interpolate pressures and displacements back and forth between the dissimilar structural and aerodynamic meshes. The ability to use different meshes for the structural and aerodynamic domains allows one to refine in each domain in a way which is more appropriate for the type of solver used in each discipline. An example of the utility of this is given below.

In previous LCO computations for the configuration by Gordnier (2003) and Gordnier and Melville (1999), two separate nonlinear mechanisms were responsible for limiting the growth of the wing oscillation. In Gordnier and Melville (1999), the structural model was linear and the nonlinear mechanism was in the aerodynamics. Here the flutter instability caused the growth of the motion of the wing. Since for this configuration the flutter mode is a coupled bending-torsion motion, the torsional component produces a nonzero local angle of the wing. Once the local angle of attack reaches a certain level it produces a leading edge vortex. This leading edge vortex in turn produces a normal force, $180°$ out of phase with the motion of the wing, which acts to limit the motion and cause the LCOs. It should be noted, in these computations shock waves also formed inboard of the leading edge vortex.

In Gordnier (2003), the nonlinear von Karman structural model was used which produced an entirely different LCO mechanism. In this work the dominant nonlinearity was structural and the LCO mechanism was the stiffening of the structure due to the nonlinear coupling of the in-plane and out-of-plane deflections.

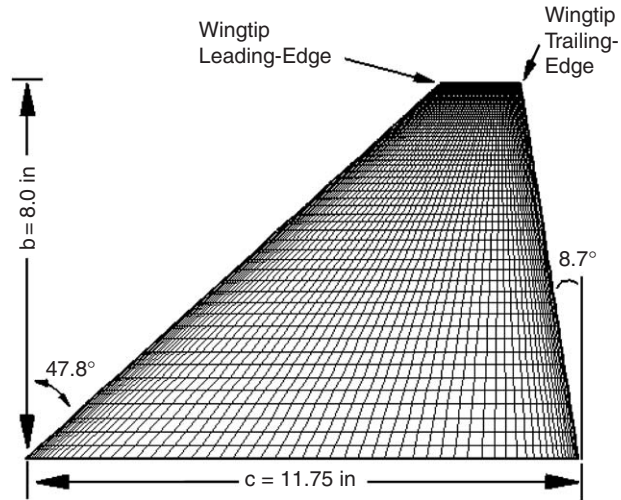[1] 1 kg = 2.2046 lbm; 1 in = 2.54 cm.
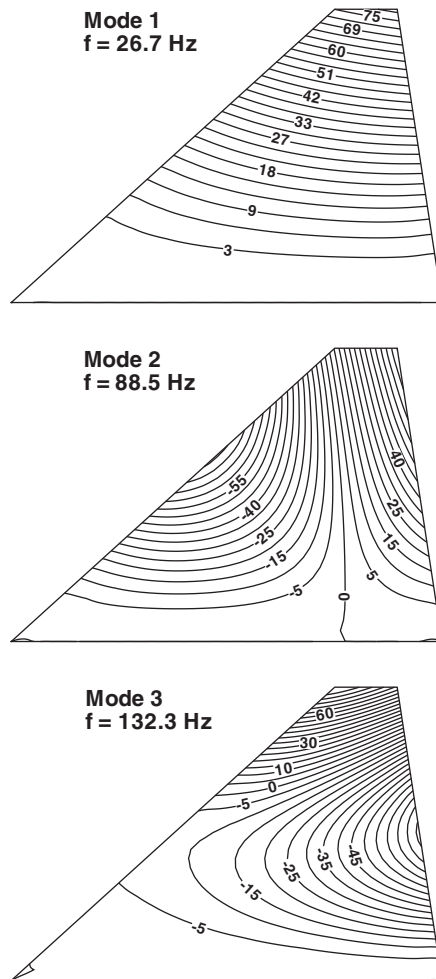
Fig. 1. Schematic of the cropped delta wing.

Fig. 2. Delta wing mode shapes.

In the current investigation, computations were performed for an initially nonlifting wing($\alpha = 0$) in transonic flow at a series of freestream dynamic pressures. At each dynamic pressure, the simulation is started from a steady flow solution obtained at zero angle of attack. The initial condition given to the structure is a nonzero structural velocity in the first bending mode of the wing.

In Figs. 3 and 4 the delta wing LCO amplitudes and LCO frequencies are shown for three separate computational models, two from Gordnier (2003) and those computed using the higher fidelity structural model presented here. Also shown are the experimental results of Schairer and Hand (1997). The LCO results are presented for the wing motion at the trailing edge tip. As was the case in the models used in the previous work, the current model correctly predicts the
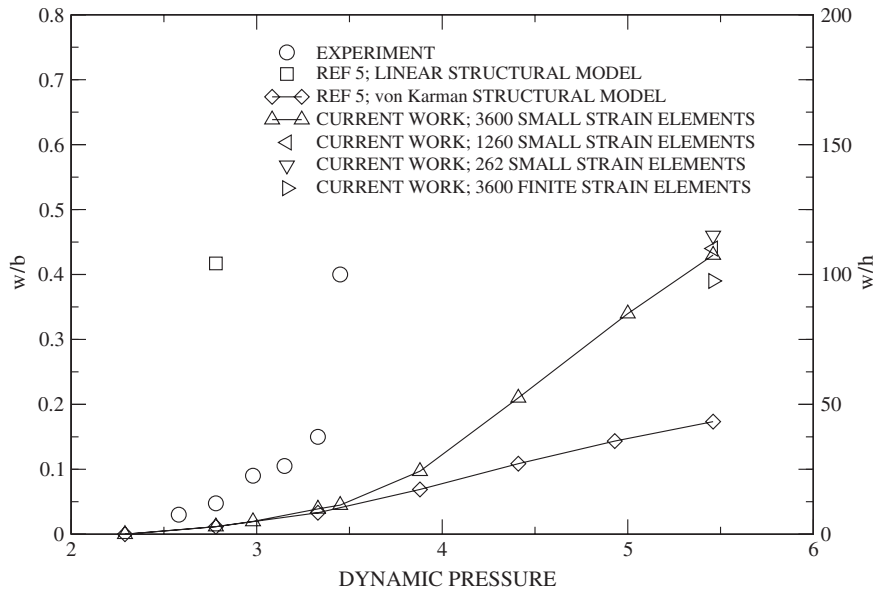
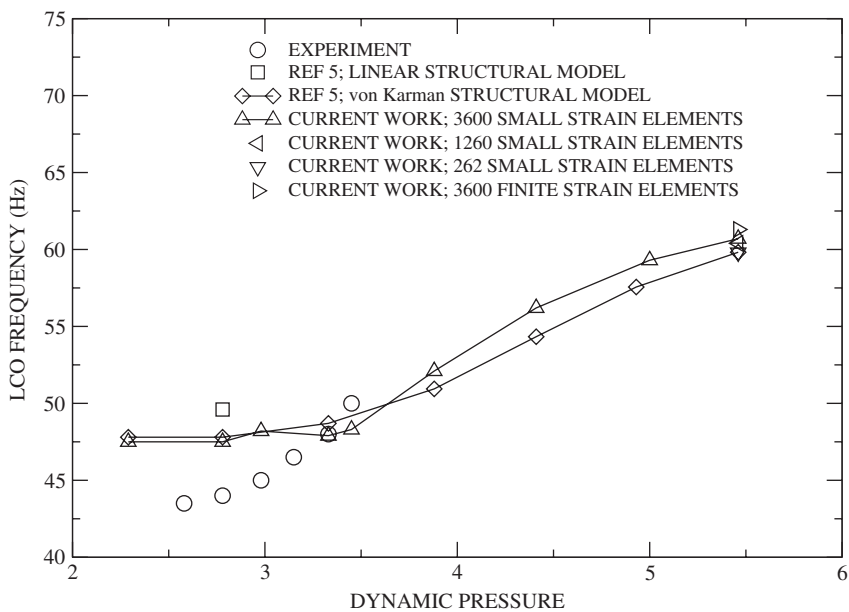Fig. 3. Delta wing wingtip trailing edge LCO amplitude.

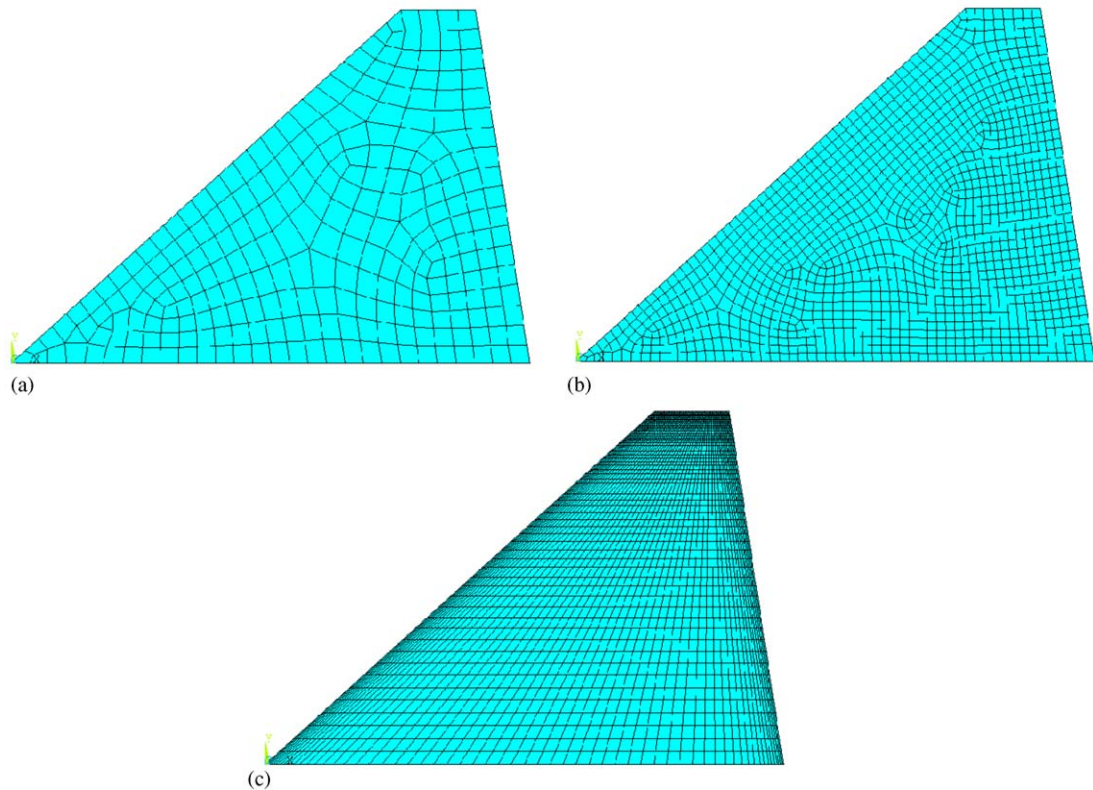Fig. 4. Delta wing wingtip trailing edge LCO frequency.

Fig. 5. Structural meshes: (a) unstructured mesh with 262 elements; (b) unstructured mesh with 1260 elements; (c) baseline structured mesh with 3600 elements.

flutter dynamic pressure. This is not surprising since here the onset of flutter is not predicated on the fidelity of the nonlinear structural model.

In Figs. 3 and 4, for the range of dynamic pressures for which experimental results are reported, there is little difference in the LCO magnitudes and frequencies computed with the current computational model and those computed with the nonlinear von Karman model used in Gordnier (2003). Apparently, in this range of dynamic pressures, the model rotations due to LCO are small enough that the assumptions made in von Karman theory are still valid. Unfortunately, this also results in minimal improvement in the theoretical and experimental correlation for this configuration.

Differences in the LCO amplitudes computed using the von Karman model of Gordnier (2003) and the current model start to become noticeable at a dynamic pressure of 3.88 psi. At a dynamic pressure of 5.46 psi the LCO magnitude computed using the current model is more than twice that computed by the model in Gordnier (2003). This behavior results in a LCO curve which is qualitatively in better agreement with the experiment. The LCO curve of Gordnier (2003) shows a linear increase in LCO amplitude with dynamic pressure while in both the experiment and current theoretical model this trend is nonlinear.

While the current model LCO amplitude results at the higher dynamic pressures differ significantly from those reported in Gordnier (2003), the LCO frequencies do not. This is counterintuitive, since one would think the von Karman model would predict higher frequencies due to its overestimation of the nonlinear stiffening. However, this behavior was also noted in Attar et al. (2004a) which compared the co-rotational model used in this work to a von Karman structural model similar to that used in Gordnier (2003).

It was found that the convergence properties of the Newton–Raphson solution of the nonlinear structural equations was poor for the baseline model at dynamic pressures larger than 3.33 psi. This was thought to be caused by an ill-conditioned system of equations. In an attempt to alleviate this problem two different approaches were sought. The first was to use different structural meshes which contained better shaped elements. As was mentioned previously, the baseline structural mesh was the same as the aerodynamic mesh on the surface of the wing. This mesh had a good deal

of refinement along the leading edge of the wing in order to capture the large gradients in the fluid variables which are expected to occur there. While the high aspect ratio cells are not a problem in the finite difference solution of fluid equations of motion, they may adversely effect the convergence of the finite element solution of nonlinear structural equations of motion. Two unstructured meshes, with better shaped elements, were used to compute LCO results at a dynamic pressure of 5.46 psi. The two unstructured meshes are shown in Fig. 5. For reference, the baseline mesh is also shown in Fig. 5. The corresponding LCO amplitudes and frequencies for the two models are shown in Figs. 3 and 4 and
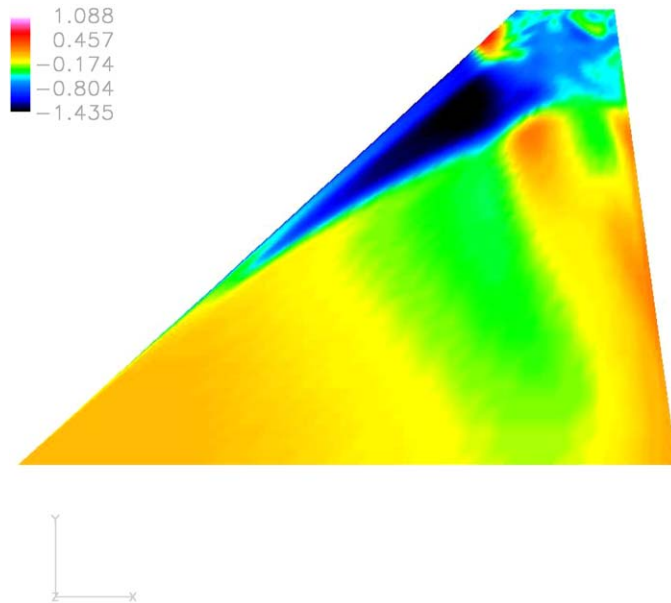

Fig. 6. Delta wing pressure coefficient contours at a dynamic pressure of 5.46 psi computed with the current theoretical model.
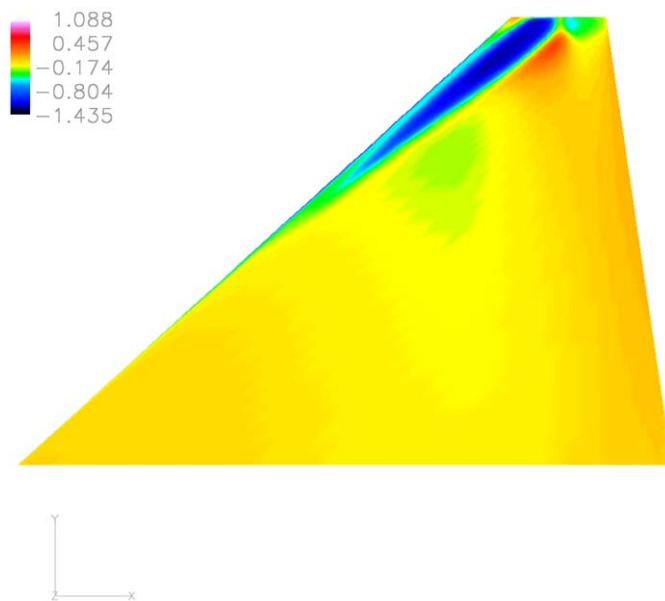

Fig. 7. Delta wing pressure coefficient contours at a dynamic pressure of 5.46 psi computed using the von Karman model of Gordnier (2003).
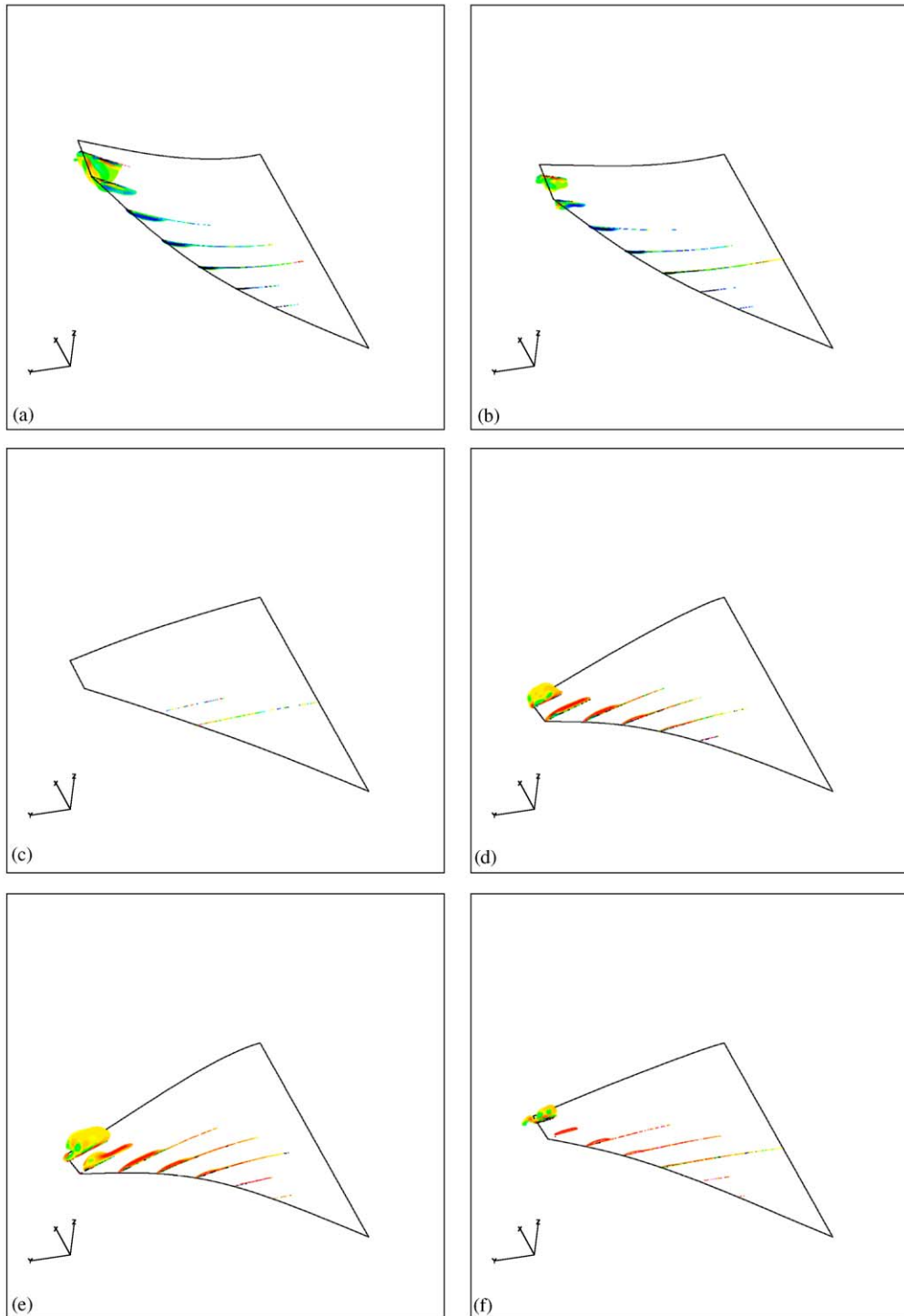
Fig. 8. Development of leading edge vortex at a dynamic pressure of 5.46 psi.

agree well with the baseline mesh results. Also, no ill-conditioning occurred in the model, which resulted in good convergence behavior (1–2 iterations per fluid–structure subiteration) of the Newton–Raphson solution of the nonlinear structural equations.
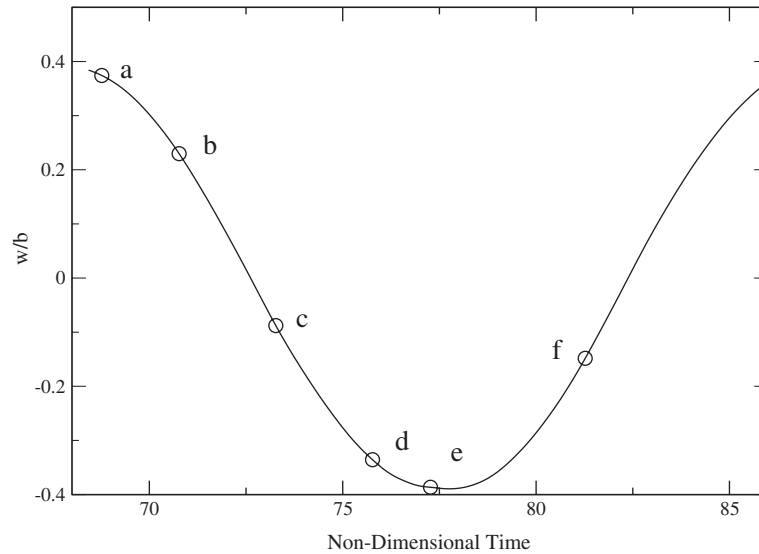
Fig. 9. Temporal location of portions of Fig. 8.

The second approach uses a different shell element which no longer employs a small strain, co-rotational formulation. A finite strain element using an updated Lagrangian method to compute the model stiffness, the ANSYS shell181 element, was selected for this purpose. The theoretical development for this element can be found in ANSYS (2002). This model also differs from the baseline model in that a correction is made to the tangent stiffness matrix due to follower pressure loading. See Section 6.5.2 of Bonet and Wood (1997) for details on the stiffness correction due to the follower load. Results computed using this element and the baseline mesh are reported in Figs. 3 and 4. The LCO amplitude at a dynamic pressure of 5.46 psi was approximately 10% less than the baseline case. While this model used the baseline mesh with the high aspect ratio elements, the convergence of the Newton–Raphson solution remained very good, requiring only 1–2 Newton–Raphson iterations per fluid–structural subiteration. Since the computed strains were on the order of 10^{-3} which should be well within the limits of small strain theory, the difference in the LCO results are likely attributable to the stiffness correction due to follower pressure loading.

At the higher dynamic pressures, the large differences in the LCO amplitudes between the current model and the one used in Gordnier (2003) result in the strengthening of flow features which are caused by the deflection and rotation of the wing. Figs. 6 and 7 plot the pressure coefficient on the bottom surface of the wing at a dynamic pressure of 5.46 psi. In these figures the wing is at the peak of the upstroke motion of the LCO. A low-pressure region can be seen in both figures resulting from the formation of a leading edge vortex. The formation of this leading edge vortex is due to the nonzero local angle of attack induced by the torsional component of the wing LCO. The vortex in Fig. 6 is much stronger than the vortex in Fig. 7. This strengthening is the result of the current model predicting a much larger wing deflection and rotation at this dynamic pressure.

Fig. 8 displays the contours of the axial (x) component of vorticity on cross-planes from $x/c = 0.25$ to 0.90 during one half of the LCO starting at the peak of the wing upstroke. Fig. 9 gives the temporal location of each portion of the figure. Note that the vortex which exists on the bottom of the wing in Fig. 8(a) and (b) disappears in Fig. 8(c) and then reforms on the top of the wing in Fig. 8(d)–(f). One should note that unlike a rigid wing, the leading edge vortex forms downstream of the apex. This is due to the local angle of attack increasing along the leading edge. Also of importance is the breakdown of the leading edge vortex near the trailing edge of the wing (Fig. 8(a), (b), (d) and (e)). Breakdown of the leading edge vortex can be detrimental if the resulting flow interacts with downstream control surfaces.

The larger deflections computed with the current model at the larger dynamic pressures also produce shocks, Fig. 10. This figure shows the pressure coefficient contours at the spanwise plane $y/b = 0.35$ for the peak of the upstroke motion of the LCO at a dynamic pressure of 5.46 psi.
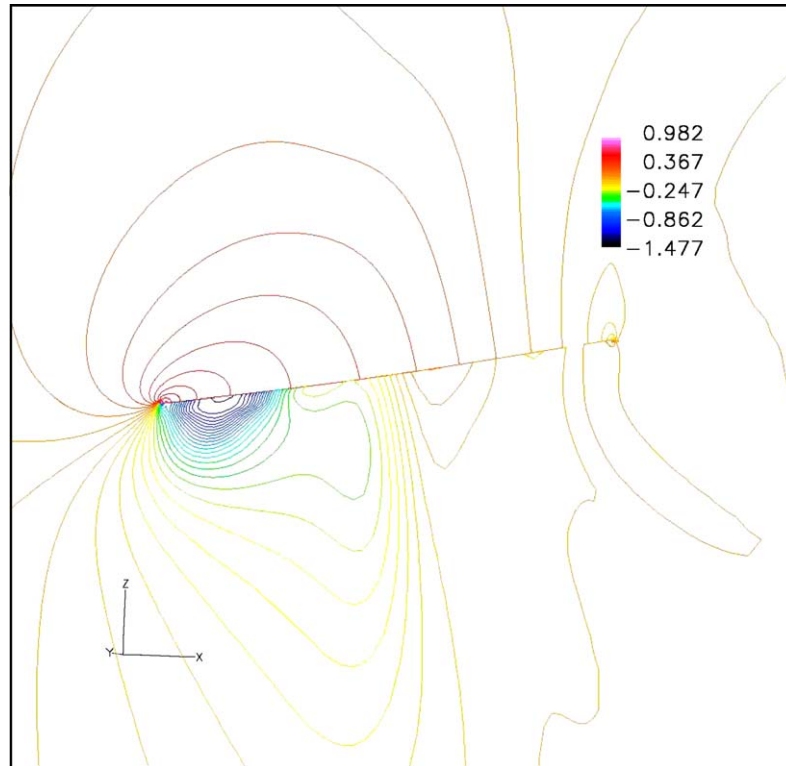
Fig. 10. Pressure coefficient contours on a spanwise plane of $y/b = 0.36$.

4. Conclusions

A new nonlinear aeroelastic solver has been described. This aeroelastic solver couples a well-validated finite-difference Euler fluid solver to a high-fidelity, finite element structural solver. The structural solver uses a co-rotational formulation to accurately predict large deflection and rotations. The two solvers are implicitly coupled via global subiterations which results in a second-order accurate (in time) aeroelastic solver.

The new aeroelastic solver is used to compute the LCO of a cropped delta wing in transonic flow. Previously, the LCOs of this configuration were computed using either a linear structural model or a lower fidelity nonlinear structural model. The results computed using the aeroelastic model which used a linear structural solver compared poorly, both qualitatively and quantitatively, with experiment. When a nonlinear von Karman structural model was used to predict the LCOs of this configuration, the correlation between theory and experiment improved.

Using the current aeroelastic solver the quantitative agreement between theory and experiment is not significantly improved over the range of dynamic pressures for which experimental results are reported. However at higher dynamic pressures the LCO amplitudes computed using the current model and the model which uses von Karman theory start to deviate from each other. The higher-order treatment of large rotation in the current structural model allows for a more accurate prediction of the large amplitude LCOs at these higher dynamic pressures. As a result of these differences in LCO magnitudes at the higher dynamic pressures, flow features which are dependent on the structural deflection and rotation of the wing are strengthened using the current model. An example of this is the strength of the leading edge vortex which forms on the upper and lower surfaces of the wing as it goes through a LCO.

LCO results were also computed using the nonlinear co-rotational finite element model for two different structural meshes which contained less (and better shaped) structural elements. A thin-plate spline routine was used to interpolate displacements and pressures between the dissimilar structural and fluid meshes. The LCO magnitudes computed using these two meshes compared well with the baseline case. In addition, better convergence of the nonlinear structural solver was noted for these two meshes due to the improved structural mesh quality.

An additional LCO computation was performed at a dynamic pressure of 5.46 psi using the baseline mesh and a finite strain element which employed an updated Lagragian methodology for computation of the nonlinear structural stiffness. The finite strain element also takes into account corrections in the stiffness matrix due to the follower nature of the pressure loading. The LCO magnitude computed with this model was approximately 10% less than the baseline case. Use of this element also resulted in improved convergence characteristics of the nonlinear structural solver, with only 1–2 Newton–Raphson iterations needed per fluid–structural subiteration.

Along with quantifying the aeroelastic behavior of the cropped delta wing configuration examined in the current work, this study also shows the importance of modelling both the fluid and structural problems with high accuracy. If care is not taken in this regard, important physics could be missed which can result in inaccurate modelling predictions. While "error margins" in the flutter/LCO flight envelopes are always present, these margins are often put into place with the idea that all the important physics is being captured and only non-deterministic details are not considered. Furthermore, because the problem is one of coupled physics, it would appear to be very difficult to determine a priori which of the domains, fluid or structural, need to be modelled with high fidelity. This would seem to be especially true for the new breed of unmanned aircraft which employ highly flexible wings.

Acknowledgments

References

ANSYS, 2002. ANSYS User Manual, Release 7.1. Swanson Analysis Systems, Inc.

Attar, P., Dowell, E., Tang, D., 2003a. Modeling aerodynamic nonlinearities for two aeroelastic configurations: delta wing and flapping flag. In: 44th AIAA/ASME/ASCE/AHS/ASC Structures, Structural Dynamics, and Materials Conference, No. 1402.

Attar, P., Dowell, E., Tang, D., 2003b. Theoretical and experimental investigation of the effects of a steady angle of attack on the nonlinear flutter of a delta wing plate model. Journal of Fluids and Structures 17, 243–259.

Attar, P., Dowell, E., White, J., 2004a. Modeling the LCO of a delta wing using a high fidelity structural model. Journal of Aircraft 42 (5), 1209–1217.

Attar, P., Dowell, E., White, J., 2004b. Modeling the LCO of a delta wing using a high fidelity structural model. AIAA Paper 2004-1402.

Beam, R., Warming, R., 1978. An implicit factored scheme for the compressible Navier–Stokes equations. AIAA Journal 16 (4), 393–402.

Bonet, J., Wood, R.D., 1997. Nonlinear Continuum Mechanics for Finite Element Analysis. Cambridge University Press, Cambridge.

Cook, R., Malkus, D., Plesha, M., Witt, R., 2002. Concepts and Applications of Finite Element Analysis, fourth ed. Wiley, New York.

Gaitonde, D., Edwards, J., Shang, J., 1995. The computed structure of a 3-D turbulent interaction caused by a cylinder/offset flare juncture. AIAA Paper 1995-0230.

Gordnier, R., 2003. Computation of limit-cycle oscillations of a delta wing. Journal of Aircraft 40 (6), 1206–1207.

Gordnier, R., Melville, R., 1999. Physical mechanisms for limit-cycle oscillations of a cropped delta wing. AIAA Paper 99-3796, Presented at the 30th AIAA Fluid Dynamics Conference in Norfolk VA, June 28–July 1, 1999.

Gordnier, R., Visbal, M., 1991. Numerical simulation of the unsteady vortex structure over a delta wing. AIAA Paper 1991-1811.

Gordnier, R., Visbal, M., 2002. Development of a three-dimensional viscous aeroelastic solver for nonlinear panel flutter. Journal of Fluids and Structures 16 (4), 497–527.

Jameson, A., Schmidt, W., Turkel, E., 1981. Numerical solutions of the Euler equations by finite volume methods using Runge–Kutta time-stepping schemes. AIAA Paper 1981–1259.

Melville, R., Morton, S., Rizzetta, D., 1997. Implementation of a fully-implicit, aeroelastic Navier–Stokes solver. AIAA Journal 1997–2039.

Morton, S., Melville, R., Visbal, M., 1997. Accuracy and coupling issues of aeroelastic Navier–Stokes solutions on deforming meshes. AIAA Journal 1997–1085.

Nour-Omid, B., Rankin, C., 1991. Finite rotation analysis and consistent linearization using projectors. Computer Methods in Applied Mechanics and Engineering 93, 353–384.

Novozhilov, V., 1953. Foundations of the Nonlinear Theory of Elasticity. Dover, New York.

Pulliam, T., Chaussee, D., 1981. A diagonal form of an implicit approximate-factorization algorithm. Journal of Computational Physics 39 (2), 347–363.

Pulliam, T., Steger, J., 1980. Implicit finite difference simulation of three-dimensional compressible flows. AIAA Journal 18 (2), 159–167.

Schairer, E., Hand, L., 1997. Measurement of unsteady aeroelastic model deformation by stereo photogrammetry. AIAA Paper 1997-2217.

Tang, D., Dowell, E., 2001. Effects of angle of attack on nonlinear flutter of a delta wing. AIAA Journal 39 (1), 15–21.

Tang, D., Henry, J., Dowell, E., 1999. Limit cycle oscillations of delta wing models in low subsonic flow. AIAA Journal 37 (1), 155–164.